Supporting Information

Feng et al. 10.1073/pnas.1717870115

SI Materials and Methods

Animal Model. All animal procedures were approved by the Beth Israel Deaconess Medical Center (BIDMC) Animal Care and Use Committee. Actn4$^{K256E/K256E}$ mice were developed by BIDMC transgenic core using RNA-guided CRISPR nickase Cas9 approach as described previously (1, 2). Superovulated FVB/N females were mated with FVB/N male mice. Fertilized zygotes were collected and then microinjected with a mixture consisting of paired 100 ng/μL gRNA (PNA Bio), 200 ng/μL Cas9 D10A Nickase protein (PNA Bio), and a single-stranded 30–40 ng/μL DNA (ssDNA) oligo (IDT). Zygotes were cultured overnight, and the developing embryos were transferred the following morning to pseudopregnant recipients. The genotypes of the founder mice were verified by Sanger sequencing. A mutant male mouse was crossed with an FVB female. From the offspring of the backcross, heterozygous female and male mice were intercrossed to generate homozygous K256E knockin mice and their WT littermates. Mice were genotyped using custom-designed K256E TaqMan SNP analysis assay: guide RNA 1: AAGGGTTAAATGGCCCAAGCAGG; guide RNA 2: CACAGCCCGGCCCGACGAGAAGG; ssDNA: GTGATCTCACCCCTGCTTGGGCCATTTAACCCTTGTTGTTCACTTACAGACATCGTGAACACAGCCCGGCCCGACGAG**GAG**GCCATAATGACATATGTGTCCAGCTTCTACCATGCCTTTTC (bolded letter indicates the DNA codon change).

Measurement of Urine Albumin and Creatinine. Spot urine samples were collected from homozygous Actn4$^{K256E/K256E}$ mice and their WT littermates at ages between 3 and 7 wk. Albuminuria was measured by ELISA kit according to the manufacturers' instructions (Bethyl Laboratories). Urine creatinine was determined by mass spectrometry using methods established previously (3). Denatured urine was analyzed by SDS/PAGE using Coomassie Blue staining to detect urinary albumin.

Kidney Sections Staining. Mice kidneys were formalin-fixed and paraffin-embedded using routine protocols. Some of the 5-μm kidney sections were stained with periodic acid-Schiff and evaluated by light microscopy. Other sections were formalin-fixed, paraffin-embedded, and then deparaffinized and rehydrated, followed by antigen retrieval in heated Tris-EDTA buffer, pH 8. The sections were blocked in 5% normal donkey serum and sequentially incubated with indicated primary WT-1 (ab89901; 1:300; Abcam) and nephrin (ProGen; catalog no. GP-N2; 1:100) antibodies overnight at 4 °C. After washing in TBS, the sections were incubated with CY3-conjugated donkey anti-rabbit secondary antibody (Jackson ImmunoResearch) and Alexa 647-conjugated donkey anti-guinea pig secondary antibody (Jackson ImmunoResearch), Hoechst 33342 (Life Technologies), and mounted in Prolong Gold anti-fade mounting media (Life Technologies). The confocal images were acquired with Zeiss LSM 880 confocal microscope with a 20×, 0.8, and 63×, 1.4 oil objective lens. The image acquisition software is Zen Black (Carl Zeiss Microscopy).

Podocyte Isolation. Primary podocytes were isolated by previously described methods (4). Briefly, both kidneys were removed, minced, and sequentially pressed through 100-, 70-, and 40-μm cell strainers. The isolated glomeruli were seeded on collagen I-coated plates. After 4 days of podocyte outgrowth, podocytes were passaged and used within 3 wk since the day of isolation. Primary mice podocytes were cultured in RPMI medium (Thermo Fisher Scientific) supplemented with 10% FBS, antibiotic–antimycotic Solution (Corning), and ITS Liquid Media Supplement (Sigma) (5).

Measurement of Actin Filament Orientation Autocorrelation. Primary podocytes were allowed to adhere for 8 h before being fixed in 4% paraformaldehyde, permeabilized in 0.1% Triton X-100, and blocked with BlockAid Solution (Thermo Fisher Scientific). Podocytes were stained with rhodamine phalloidin (Thermo Fisher Scientific) to visualize their actin structure. Confocal images were acquired using a Zeiss LSM 880 confocal system equipped with a Plan-Apochromat 63×/1.40 oil objective lens. Actin filament orientation autocorrelation was quantified as previously described (6). Briefly Actin images of WT and mutant podocytes were analyzed using ImageJ plugin OrientationJ Vector field (7). Local orientation of actin filaments at each pixel in the image was calculated by obtaining the actin structure tensor of the image. Local actin orientation θ is calculated by the intensity in a region of 10 × 10 pixels bin (1 pixel = 0.19 μm). Spatial autocorrelation $C(r)$ of these averaged angles was calculated as $C(r) = \langle \cos 2(\theta_i - \theta_j(r)) \rangle$, where $0 < r < 50$ μm (8); 50 μm is the approximate average cell radius. j represents all regions within the circle radius r from the center region i. $\langle\ \rangle$ indicates calculating the average value.

Traction Force Microscopy. Podocyte contraction—manifested on the underlying substrate as traction—was quantified using the approach of traction force microscopy (TFM) (6, 9). Briefly, polyacrylamide gel substrates (Young's modulus, 26 kPa) were coated with surface-bound 0.1-μm latex sulfate-modified fluorescent red beads (Sigma), and then ligated with collagen I (Advanced Biometric). Podocytes were seeded on the collagen-ligated substrate to adhere for 4–8 h before the traction force experiments. Inverted fluorescent microscope (Leica DMI 6000) with 20× objective lens was used to acquire fluorescence images of beads directly underneath each single cell. These bead images were first taken when the cells were attached and then after the cells were removed with 10× 2.5% trypsin (VWR). The displacement of the beads was calculated using custom-written particle image velocimetry software. From the displacement field, an a priori knowledge of substrate modulus, and a manual trace of the cell boundary, traction was computed using constrained Fourier transform traction cytometry (9) From the traction map, the contractile moment (CM), μ, a scalar metric of the cell's net contractile strength, was calculated from the following equation (9): $\mu = tr(M) = M_{xx} + M_{yy}$, where M represents the first-order traction moment matrix, and M_{xx} and M_{yy} are the contributions of the cell in contracting the substrate in the x and y directions, respectively. The root-mean-squared value of traction is also reported.

Stress Microscopy. Stresses within each cell are computed using monolayer stress microscopy (10, 11), which uses the cell-to-substrate tractions and the principle of force equilibrium to determine the 2D intracellular stress for each cell. To compute these stresses, we make additional assumptions about the properties of the cell. We used 5 μm as cell height and 0.3 as the Poisson's ratio. We assume the elastic modulus to be homogeneous across the cell. Given this assumption of homogeneity, our implementation is independent of the actual value of modulus (11). Intracellular stress was calculated from individual stress tensors within the cell. We analyzed intracellular stress using two metrics, the tension σ (defined as the mean principal stress) and the

first principal orientation θ. To visualize these metrics of the stress tensors, we used arrows, with the length corresponding to the tension σ and the orientation of the arrow reflecting the orientation of principal orientation θ.

The spatial autocorrelation of tension σ was computed according to the following equation:

$$C(r) = \left(1/Ns^2\right) \int \tilde{\sigma}(x)\tilde{\sigma}(x-r)dx,$$

where N is the number of data points, s^2 is the variance of σ, and $\tilde{\sigma} = \sigma - \overline{\sigma}$, with $\overline{\sigma}$ being the mean of σ. The spatial autocorrelation of principal orientation θ was computed according to the equation $C(r) = <\cos 2(\theta_i - \theta_j(r))>$, where $0 < r < 50$ μm; 50 μm is the approximate average cell radius. Similar to the autocorrelation of actin fiber orientation, j represents any location within the circle of radius r from the center location i. $\langle\ \rangle$ indicates calculating the average value.

Imposition of External Mechanical Stretch—Cell-Mapping Rheometry. Stretch was superimposed to TFM using the approach of cell-mapping rheometry (12–14). Briefly, a hollow cylindrical indenter was lowered by a precalibrated amount upon a polyacrylamide gel to impose a uniform equibiaxial stretch. Images of the cells and fluorescent beads directly underneath the cells were recorded prestretch and poststretch of 10% strain in magnitude and 4 s for duration. Poststretch images were collected immediately after stretch, at a rate of 6 s for 30 s, and then at a rate of 10 s for 2 min and 30 s (total of 3 min following each stretch). At the end of the experiment, the cell was detached with trypsin, and a single reference image of the beads was recorded. By comparing the reference image with the experimental images, tractions were computed using TFM.

Optical Magnetic Twisting Cytometry. Cytoskeletal stiffness was measured using optical magnetic twisting cytometry (15). Briefly, ferrimagnetic beads (diameter, 4.8 μm) were ligated with the Arg–Gly–Asp (RGD) peptide, to promote preferential bead binding to integrin receptors, and added at high density (~50–100 beads in 10× microscope field of view) to individual well dishes containing confluent podocytes. After 20 min of bead incubation, the well was washed and replaced with fresh medium. The beads were subsequently magnetized and twisted using a magnitude of 20 Gauss and frequency of 0.77 Hz. From a knowledge of the imposed magnetic field and the recorded bead motion, the shear storage modulus, G', can be calculated. For each cell type, G' was measured and pooled from four to five separate wells.

Cell Transfection for Live-Cell Imaging. Mouse podocytes were transfected with p^{CMV}–LifeAct–TagRFP plasmid using Lipofectamine 3000 (Thermo Fisher Scientific). After 3 h of transfection, the cells were switched back to RPMI medium for 21 h. They were trypsinized and then seeded on collagen-1–coated polyacrylamide gel substrates (Young's modulus, 26 kPa). Podocytes were allowed to adhere for 4–8 h before live-cell actin imaging using an inverted fluorescent microscope (Leica DMI 6000) with 20× objective lens.

Detachment Assay. Following stretch, as described in *Traction Force Microscopy*, mutant and WT cells were further challenged in a detachment assay using the spinning-disk method similarly as described previously (16). Briefly, NucBlue (Thermo Fisher Scientific) was added to the culture medium to visualize cell nuclei and a cell count was thereby obtained. The culture medium was removed, and each dish was mounted within a spin coater containing a spinning-disk device and rotated at a speed of 2,500 rpm (Laurel Technology model WS-650-23B) for 30 s. During spinning, cells experience a centrifugal force in a direction normal to the bottom of the plate. The culture medium was replenished soon after the spin, and a cell count was repeated. By comparing the cell number before and after the spin, the adherent fraction of cells was quantified.

Statistical Analysis. All of the statistics were calculated by a statistic tool called R (17). Mann–Whitney U test (18) or Student t test was used to calculated difference between WT and $Actn4^{K256E/K256E}$ podocytes. The P value of detachment assay was calculated by Fisher exact test and the odd ratio was calculated using the *fisher.test()* function in R. The slope line and R^2 (coefficient of determination) of Fig. 3 *A* and *B* was calculated by simple linear regression by *lm()* function in R.

Numerical Simulations of Model Disordered Semiflexible Networks. We use the model for semiflexible gel networks developed in refs. 19–21 as a mechanical analog for the actin network (20, 22, 23). The typical response of the model networks to a (shear) deformation is computed using damped molecular dynamics, a fixed imposed strain rate and periodic boundary conditions, and obtaining the stresses from the intrafibers and interfiber forces, as described in Dataset S1. For the parameters of interest here, the response is characterized by an initial softening, followed by a stiffening regime where the derivative of the shear component τ of the stress with respect to the strain γ is $\partial\tau/\partial\gamma \propto \gamma^{\alpha}$ with $\alpha \sim 3/2$ (22, 23), and eventually by the network failure or yielding, upon increasing γ (Fig. 4 *A* and *B*). The value γ_{max} of the strain at which the network starts to yield is identified as the end of the stiffening regime. We also compute, as a function of the accumulated strain, the amount of network connections (bonds) broken or formed. The yielding or failure of the network is accompanied by a strong increase in the bond breaking with the strain, coupled or not to the formation of new bonds (Fig. 4 *A* and *B*). Here, we fix the fiber density, the cross-link density, and their spatial distribution in the gel, while we vary the fiber persistence length (and hence fiber stiffness) to analyze the effect of the fiber bending stiffness alone on the network response to strain (shear strain). In a second set of mechanical tests, we subject the model networks to an increasing amount of deformation (prestrain) before measuring the network response, to analyze the mechanical response when the networks have larger and more aligned local tensions (Fig. 4*D*). In all cases, we monitor the total shear stress τ, the fraction of stretched-out fibers (and their degree of alignment), the local stresses, including the tension, as well as the bond breaking and formation (see Dataset S1 for further details).

1. Ran FA, et al. (2013) Double nicking by RNA-guided CRISPR Cas9 for enhanced genome editing specificity. *Cell* 154:1380–1389.
2. Wang H, et al. (2013) One-step generation of mice carrying mutations in multiple genes by CRISPR/Cas-mediated genome engineering. *Cell* 153:910–918.
3. Young S, Struys E, Wood T (2007) Quantification of creatine and guanidinoacetate using GC-MS and LC-MS/MS for the detection of cerebral creatine deficiency syndromes. *Curr Protoc Hum Genet* Chap 17:Unit 17.3.
4. Mundel P, et al. (1997) Rearrangements of the cytoskeleton and cell contacts induce process formation during differentiation of conditionally immortalized mouse podocyte cell lines. *Exp Cell Res* 236:248–258.
5. Saleem MA, et al. (2002) A conditionally immortalized human podocyte cell line demonstrating nephrin and podocin expression. *J Am Soc Nephrol* 13: 630–638.
6. Feng D, Steinke JM, Krishnan R, Birrane G, Pollak MR (2016) Functional validation of an alpha-actinin-4 mutation as a potential cause of an aggressive presentation of adolescent focal segmental glomerulosclerosis: Implications for genetic testing. *PLoS One* 11:e0167467.
7. Püspöki Z, Storath M, Sage D, Unser M (2016) Transforms and operators for directional bioimage analysis: A survey. *Adv Anat Embryol Cell Biol* 219:69–93.
8. Gupta M, et al. (2015) Adaptive rheology and ordering of cell cytoskeleton govern matrix rigidity sensing. *Nat Commun* 6:7525.
9. Butler JP, Tolić-Nørrelykke IM, Fabry B, Fredberg JJ (2002) Traction fields, moments, and strain energy that cells exert on their surroundings. *Am J Physiol Cell Physiol* 282: C595–C605.
10. Tambe DT, et al. (2011) Collective cell guidance by cooperative intercellular forces. *Nat Mater* 10:469–475.

11. Tambe DT, et al. (2013) Monolayer stress microscopy: Limitations, artifacts, and accuracy of recovered intercellular stresses. *PLoS One* 8:e55172.
12. Trepat X, et al. (2007) Universal physical responses to stretch in the living cell. *Nature* 447:592–595.
13. Chen C, et al. (2010) Fluidization and resolidification of the human bladder smooth muscle cell in response to transient stretch. *PLoS One* 5: e12035.
14. Krishnan R, et al. (2009) Reinforcement versus fluidization in cytoskeletal mechanoresponsiveness. *PLoS One* 4:e5486.
15. Fabry B, et al. (2001) Scaling the microrheology of living cells. *Phys Rev Lett* 87: 148102.
16. García AJ, Huber F, Boettiger D (1998) Force required to break alpha5beta1 integrin-fibronectin bonds in intact adherent cells is sensitive to integrin activation state. *J Biol Chem* 273:10988–10993.
17. R Core Team (2016) *R: A Language and Environment for Statistical Computing* (R Foundation for Statistical Computing, Vienna).
18. Mann HB, Whitney DR (1947) On a test of whether one of two random variables is stochastically larger than the other. *Ann Math Stat* 18:50–60.
19. Bouzid M, Colombo J, Barbosa LV, Del Gado E (2017) Elastically driven intermittent microscopic dynamics in soft solids. *Nat Commun* 8:15846.
20. Bouzid M, Del Gado E (October 4, 2017) Network topology in soft gels: Hardening and softening materials. *Langmuir*, 10.1021/acs.langmuir.7b02944.
21. Colombo J, Del Gado E (2014) Stress localization, stiffening, and yielding in a model colloidal gel. *J Rheol (NYNY)* 58:1089–1116.
22. Gardel ML, et al. (2004) Elastic behavior of cross-linked and bundled actin networks. *Science* 304:1301–1305.
23. Broedersz CP, Mackintosh FC (2014) Modeling semiflexible polymer networks. *Rev Mod Phys* 86:995–1036.

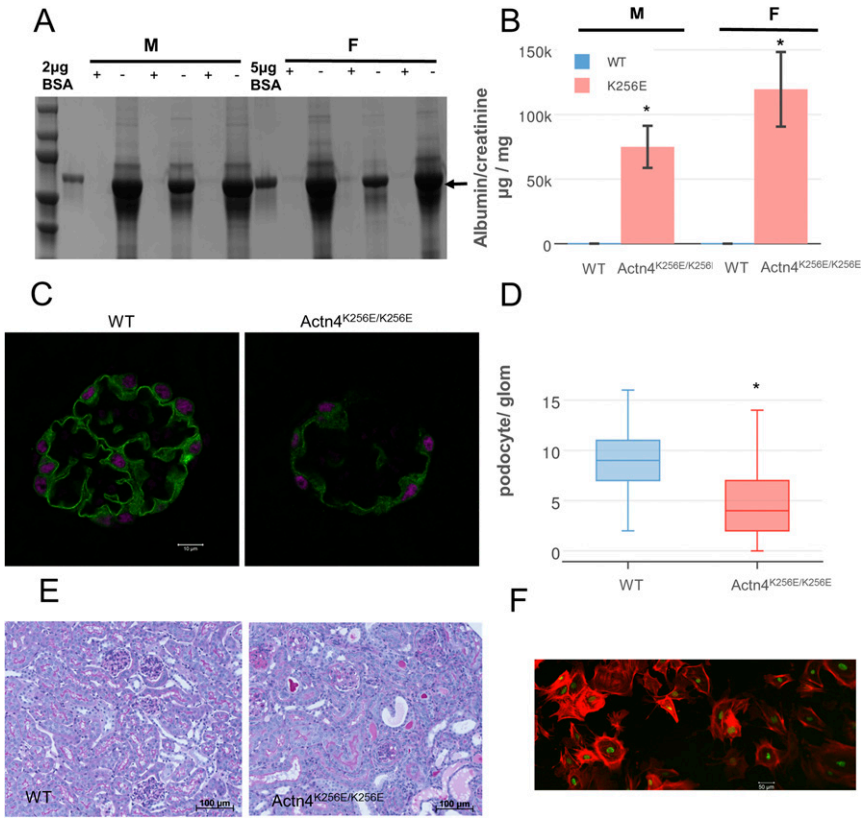

Fig. S1. Homozygous K256E knockin Actn 4 (Actn4$^{K256E/K256E}$) mice exhibit albuminuria and podocyte loss. (*A*) SDS/PAGE gel stained by Coomassie Blue was used to detect urinary albumin from representative male and female WT and Actn4$^{K256E/K256E}$ mice ($n = 3$ per group). Plus (+) signifies WT mice, and minus (–) signifies Actn4$^{K256E/K256E}$. Compared with WT, Actn4$^{K256E/K256E}$ mice demonstrated more albuminuria shown by enhanced albumin staining at 67 kDa (indicated by arrow). (*B*) Urine was collected from WT ($n = 5$ males and 5 females) and Actn4$^{K256E/K256E}$ mice ($n = 5$ males and 5 females) between 4 and 7 wk of age, and albumin/creatinine ratio (in micrograms per milligram) was measured. *$P < 0.05$ indicates significant difference between WT and Actn4$^{K256E/K256E}$ of the same gender. For male, mean ± SE: WT, 67 ± 9, vs. Actn4$^{K256E/K256E}$, 16,770 ± 16,262. For female, mean ± SE: WT, 49 ± 6, vs. Actn4$^{K256E/K256E}$, 36,880 ± 28,897. (*C*, *Left*) Representative immunofluorescence staining of nephrin and WT-1 in female WT and Actn4$^{K256E/K256E}$ mouse glomeruli. Green indicates nephrin, and purple indicates WT-1 (magnification, 63×). (Scale bar: 10 μm.) (*D*) Quantification of podocyte number (indicated by WT-1-positive staining) per glomeruli on each kidney section ($n = 3$ WT and 3 Actn4$^{K256E/K256E}$ mice). In total, 189 WT and 155 Actn4$^{K256E/K256E}$ glomeruli were quantified. Compared with WT, Actn4$^{K256E/K256E}$ had significantly fewer podocytes per glomerulus per section at 4–5 wk of age (mean ± SE: WT, 8.9 ± 0.2, vs. Actn4$^{K256E/K256E}$, 4.4 ± 0.3). *$P < 0.05$ indicates significant difference between WT and Actn4$^{K256E/K256E}$. (*E*) Representative kidney sections from 4-wk-old WT and mutant mice, stained with periodic acid–Schiff, and photographed at 20× magnification. Glomerulosclerosis is visible in the kidneys of Actn4$^{K256E/K256E}$ mice by histopathologic examination. (Scale bar: 100 μm.) (*F*) Immunostaining image of WT-1 (green) and actin (red) and photographed at 20× magnification. The isolated podocyte expressed podocyte-specific marker WT-1. (Scale bar: 50 μm.)

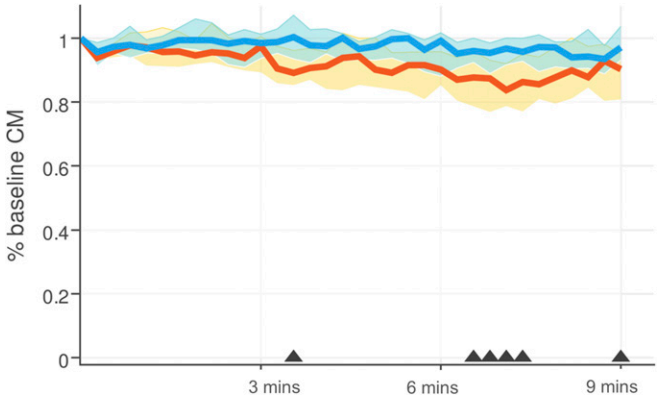

Fig. S2. Single-podocyte spreading area in response to three transient stretches over time. The *y* axis plots individual podocyte spreading area normalized by their baseline spreading area before stretch, while the *x* axis plots serial time points relative to the three transient stretches with 3, 6, and 9 min indicating the end of the 3-min recovery phase after each stretch. Graphed values represent the median (lines) and interquartile ranges (shaded areas). The black triangles along the *x* axis indicate the time points where there is a significant difference between WT (blue) and Actn4$^{K256E/K256E}$ (red) ($P < 0.05$).

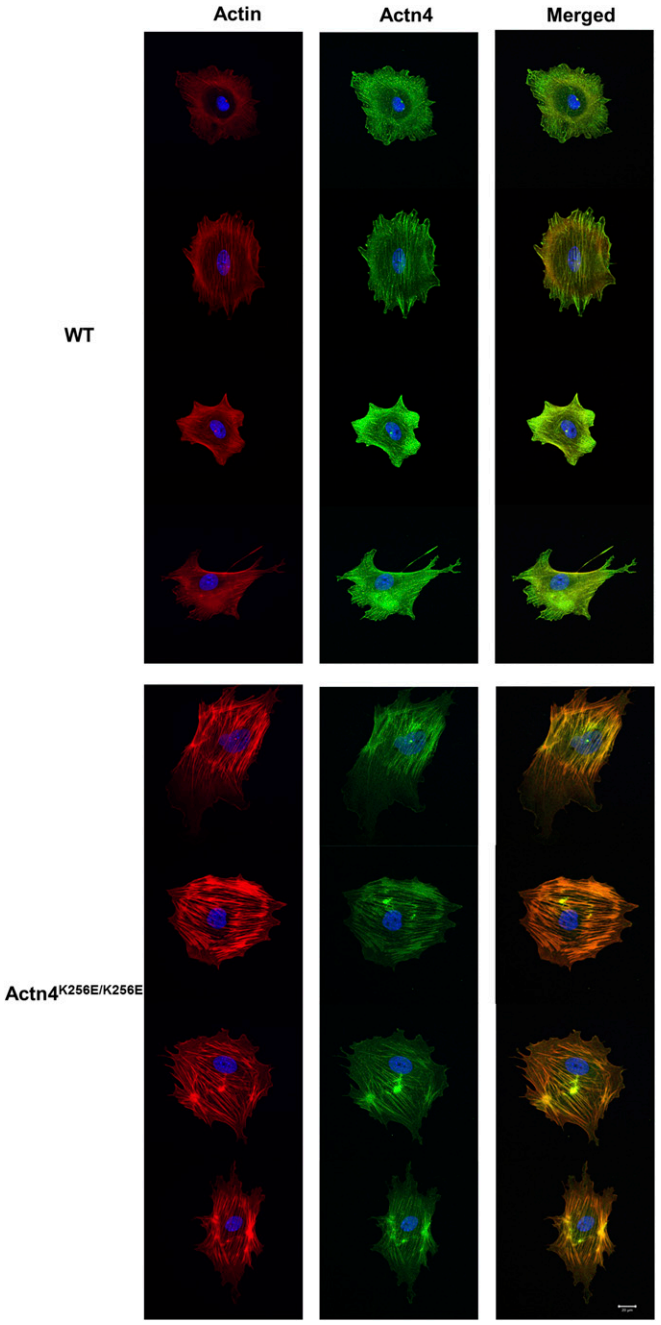

Fig. S3. Representative immunofluorescence images of actin filaments (*Left* column in red) and Actn4 (*Middle* column in green) distribution within WT ($n = 4$) and Actn4$^{K256E/K256E}$ ($n = 4$) podocytes grown on a collagen-coated coverslip (63× magnification). *Right* column shows the merged images of actin and Actn4. The quantification of the distribution of actin filament orientation within these cells along with five other WT and five other Actn4$^{K256E/K256E}$ podocytes is presented in Fig. 2*B*. (Scale bar: 20 μm.)

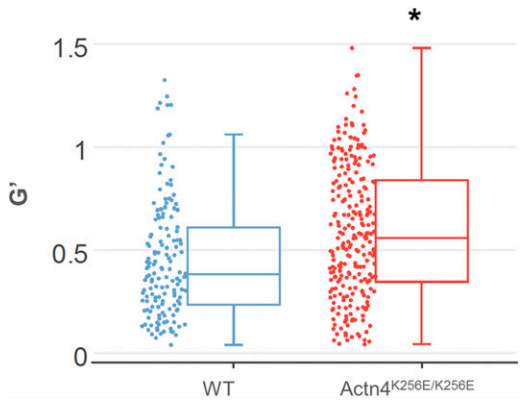

Fig. S4. The shear storage modulus, G', in pascals per nanometer of WT (blue bar) and Actn4$^{K256E/K256E}$ (red bar) podocytes. WT median (interquartile range), 0.38 (0.23–0.61), vs. Actn4$^{K256E/K256E}$, 0.56 (0.35–0.84). The differences were statistically significant (*$P < 0.05$). Data were pooled from 148 beads for WT and 248 beads for Actn4$^{K256E/K256E}$. Podocytes were isolated from one WT and one Actn4$^{K256E/K256E}$ mice.

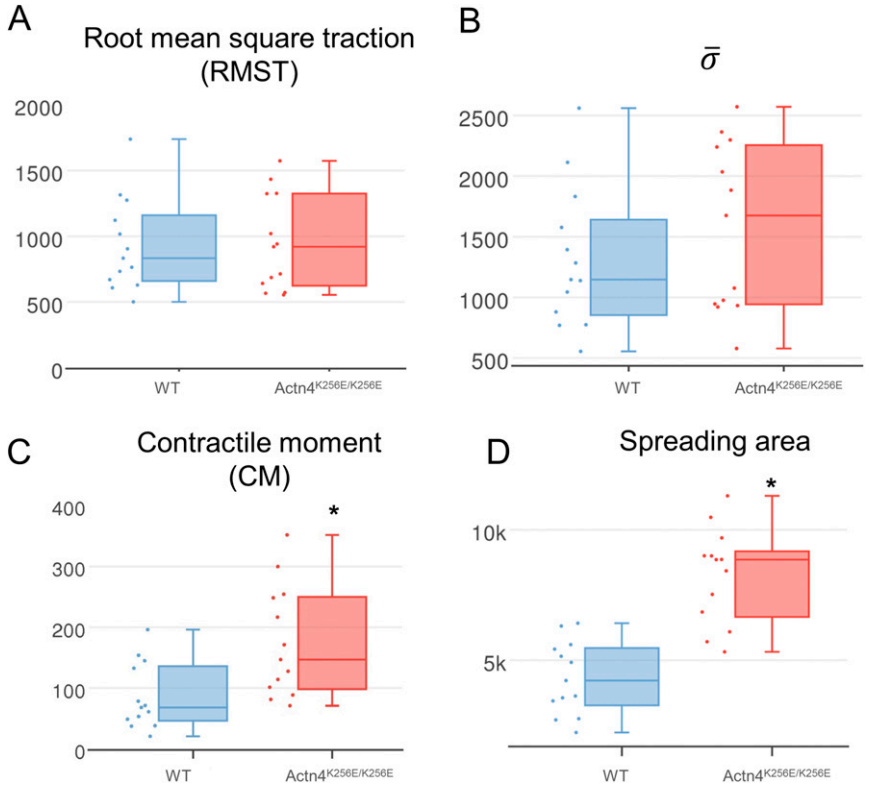

Fig. S5. Baseline root-mean-square traction (RMST) (*A*) and mean intracellular tension of the entire cell $\bar{\sigma}$ (*B*) across WT (blue bar) and Actn4$^{K256E/K256E}$ (red bar) podocytes. (*A*) RMST was not significantly different between WT and Actn4$^{K256E/K256E}$ podocytes. WT median (interquartile range), 833 (670–1,122) Pa, vs. Actn4$^{K256E/K256E}$, 920 (641–1,324) Pa. $\bar{\sigma}$ was not significantly different between WT and Actn4$^{K256E/K256E}$ podocytes. WT median (interquartile range), 1,147 (880–1,577) Pa, vs. Actn4$^{K256E/K256E}$, 1,675 (946–2,240) Pa. Baseline contractile moment (CM) (*C*) and cellular spreading area (*D*) of WT (blue bar) and Actn4$^{K256E/K256E}$ (red bar) podocytes. CM of Actn4$^{K256E/K256E}$ podocytes was significantly higher than that of WT. WT median (interquartile range), 68 (49–133) pNm, vs. Actn4$^{K256E/K256E}$, 147 (102–248) pNm. (*D*) Cellular spreading area of Actn4$^{K256E/K256E}$ podocytes was significantly higher than that of WT. WT median (interquartile range), 4,223 (3,442–5,426) μm^2, vs. Actn4$^{K256E/K256E}$, 8,855 (6,849–9,003) μm^2. *$P < 0.05$ indicates significant difference between WT and Actn4$^{K256E/K256E}$.

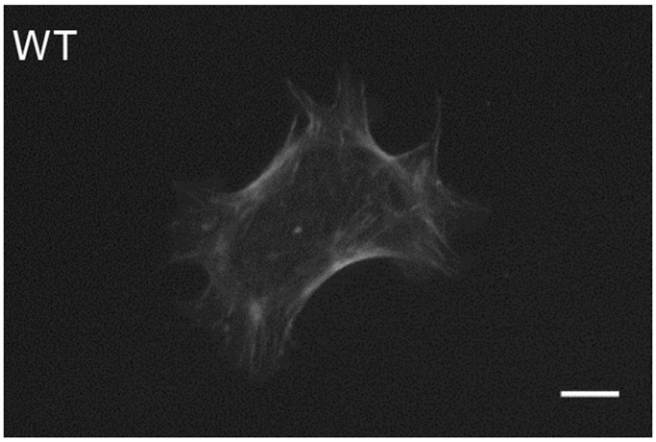

Movie S1. WT podocytes demonstrated small areas of cytoskeletal breakages after stretch that were largely repaired during the 3-min recovery period. WT podocytes were transfected with p^{CMV}–LifeAct–TagRFP plasmid using Lipofectamine 3000 (Thermo Fisher Scientific). After 3 h of transfection, the cells were switched back to RPMI medium for 21 h. They were trypsinized and then seeded on collagen-1–coated polyacrylamide gel substrates (Young's modulus, 26 kPa). Podocytes were allowed to adhere for 4–8 h before live-cell actin imaging using an inverted fluorescent microscope (Leica DMI 6000) with 20× objective lens. Images were collected at baseline, after a transient stretch, and after 3-min recovery.

Movie S1

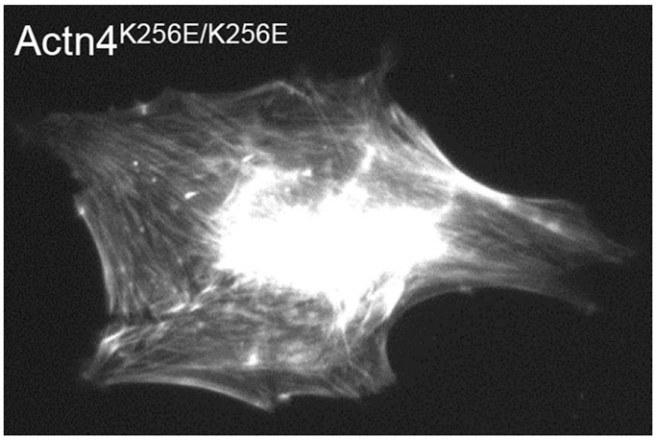

Movie S2. $Actn4^{K256E/K256E}$ podocytes demonstrated visible cytoskeletal breakages after stretch that did not repair during the 3-min recovery period. $Actn4^{K256E/K256E}$ podocytes were transfected with p^{CMV}–LifeAct–TagRFP plasmid using Lipofectamine 3000 (Thermo Fisher Scientific). After 3 h of transfection, the cells were switched back to RPMI medium for 21 h. They were trypsinized and then seeded on collagen-1–coated polyacrylamide gel substrates (Young's modulus, 26 kPa). Podocytes were allowed to adhere for 4–8 h before live-cell actin imaging using an inverted fluorescent microscope (Leica DMI 6000) with 20× objective lens. Images were collected at baseline, after a transient stretch, and after 3-min recovery.

Movie S2

Other Supporting Information Files

Dataset S1 (PDF)